Chemical Research in Toxicology

Article

pubs.acs.org/crt

DNA Sequence Modulates Geometrical Isomerism of the *trans*-8,9-Dihydro-8-(2,6-diamino-4-oxo-3,4-dihydropyrimid-5-yl-formamido)-9-hydroxy Aflatoxin B_1 Adduct

Liang Li, Kyle L. Brown, Ruidan Ma, and Michael P. Stone*

Department of Chemistry, Center in Molecular Toxicology, Center for Structural Biology, and the Vanderbilt-Ingram Cancer Center, Vanderbilt University, Nashville, Tennessee 37235, United States

Supporting Information

ABSTRACT: Aflatoxin B_1 (AFB_1), a mycotoxin produced by *Aspergillus flavus*, is oxidized by cytochrome P450 enzymes to aflatoxin B_1-8,9-epoxide, which alkylates DNA at *N*7-dG. Under basic conditions, this *N*7-dG adduct rearranges to yield the *trans*-8,9-dihydro-8-(2,6-diamino-4-oxo-3,4-dihydropyrimid-5-yl-formamido)-9-hydroxy aflatoxin B_1 (AFB_1–FAPY) adduct. The AFB_1–FAPY adduct exhibits geometrical isomerism involving the formamide moiety. NMR analyses of duplex oligodeoxynucleotides containing the 5′-XA-3′, 5′-XC-3′, 5′-XT-3′, and 5′-XY-3′ sequences (X = AFB_1–FAPY; Y = 7-deaza-dG) demonstrate that the equilibrium between *E* and *Z* isomers is controlled by major groove hydrogen bonding interactions. Structural analysis of the adduct in the 5′-XA-3′ sequence indicates the preference of the *E* isomer of the formamide group, attributed to formation of a hydrogen bond between the formyl oxygen and the N^6 exocyclic amino group of the 3′-neighbor adenine. While the 5′-XA-3′ sequence exhibits the *E* isomer, the 5′-XC-3′ sequence exhibits a 7:3 *E*:*Z* ratio at equilibrium at 283 K. The *E* isomer is favored by a hydrogen bond between the formyl oxygen and the N^4-dC exocyclic amino group of the 3′-neighbor cytosine. The 5′-XT-3′ and 5′-XY-3′ sequences cannot form such a hydrogen bond between the formyl oxygen and the 3′-neighbor T or Y, respectively, and in these sequence contexts the *Z* isomer is favored. Additional equilibria between α and β anomers and the potential to exhibit atropisomers about the C5–N^5 bond do not depend upon sequence. In each of the four DNA sequences, the AFB_1–FAPY adduct maintains the β deoxyribose configuration. Each of these four sequences feature the atropisomer of the AFB_1 moiety that is intercalated above the 5′-face of the damaged guanine. This enforces the R_a axial conformation for the C5–N^5 bond.

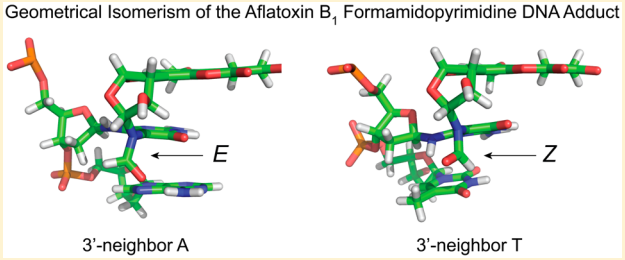

INTRODUCTION

Aflatoxin B_1 (AFB_1, **1**, Scheme 1) is a mycotoxin that is isolated from *Aspergillus flavus* and which contaminates agricultural products.[1−4] AFB_1 is a mutagen in bacteria[2,5−7] and in mammalian cells.[8] It is a carcinogen in fish[9] and rodents.[10−12] Dietary exposures to AFB_1 are high in areas of Asia[13,14] and sub-Saharan Africa.[15,16] Epidemiological studies suggest that chronic exposure to AFB_1 is a contributing factor in the etiology of hepatitis B virus (HBV) associated hepatocellular carcinomas (HCC).[4,14,17−19] Effective biomarkers allowing quantitation of human dietary exposures to AFB_1 have been identified,[14,20,21] and there have been efforts to develop chemopreventive interventions to chronic exposures.[14,22−25]

AFB_1 is metabolized by cytochrome P_{450} 3A4[26−29] to yield AFB_1-*exo*-8,9-epoxide (Scheme 1).[30] The efficiency of adduction at *N*7-dG by this epoxide[31] is attributed to its intercalation on the 5′-face of guanine.[32−35] This facilitates the formation of *trans*-8,9-dihydro-8-(*N*7-guanyl)-9-hydroxy aflatoxin B_1.[36−38] This cationic adduct depurinates to release AFB_1–guanine,[36] or alternatively, undergoes base-catalyzed opening of the imidazole ring forming the *trans*-8,9-dihydro-8-(2,6-diamino-4-oxo-3,4-dihydropyrimid-5-yl-formamido)-9-hydroxy aflatoxin B_1 (AFB_1–FAPY) adduct.[39−41]

The AFB_1–FAPY adduct[41] (Scheme 1) is of interest because the genotoxicity of AFB_1 is ascribed primarily to this adduct. It induces G → T transitions[42] associated with AFB_1 mutagenesis in bacteria[6,42] and mammalian cells.[8] The cationic *N*7-dG AFB_1 adduct exhibits a similar spectrum of mutations but at lower levels.[43,44] Moreover, the AFB_1–FAPY adduct is persistent in vivo.[39,45,46] It may be linked to G → T transversions in the tumor suppression gene p53[47−54] and *ras* proto-oncogenes.[55] Smela et al.[42] have demonstrated that the AFB_1–FAPY adduct equilibrates between two species, one of which is mutagenic whereas the other blocks DNA replication. These are α and β deoxyribose anomers.[41] In duplex DNA, the β anomer is favored, but in single-strand DNA, the equilibrium shifts to favor the α anomer.[41] At the nucleoside level, the AFB_1–FAPY adduct exhibits atropisomerism about the C5–N^5 bond.[41] This has not been observed in duplex DNA, probably because both deoxyribose anomers of the adduct intercalate with the AFB_1

Received: September 17, 2014
Published: January 14, 2015

DOI: 10.1021/tx5003832
Chem. Res. Toxicol. 2015, 28, 225−237

Scheme 1. Formation of the *trans*-8,9-Dihydro-8-(2,6-diamino-4-oxo-3,4-dihydropyrimid-5-yl-formamido)-9-hydroxy Aflatoxin B_1 Adduct (AFB_1−FAPY Adduct) and Numbering of the AFB_1 Protons

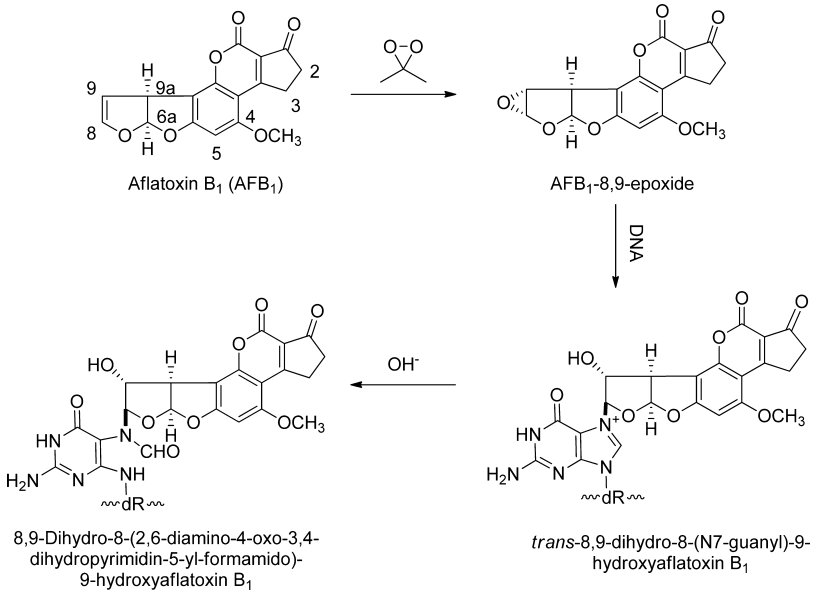

moiety on the 5′ face of the adducted nucleotide,[56−58] similar to the *N*7-dG cationic adduct.[34,57,59,60] This enforces the R_a axial conformation for the C5−N^5 bond.[56−58] Additionally, the AFB_1−FAPY adduct exhibits geometrical isomerism involving the formamide moiety.[41] In the 5′-XA-3′ sequence,[56−58] the potential for a hydrogen bond between the formyl oxygen and the N^6 exocyclic amino group of the 3′-neighbor adenine has been recognized, and this has been proposed to explain the preference of the *E* isomer as opposed to the *Z* isomer of the formamide moiety.[40,41] This suggests that the orientation of the formamide moiety is controlled by differential hydrogen bonding opportunities in the DNA major groove, and the equilibrium between *E* and *Z* isomers of the formamide moiety is sequence dependent.

To characterize how DNA sequence modulates the conformation of the AFB_1−FAPY formamide moiety, four oligodeoxynucleotide duplexes containing the 5′-XA-3′, 5′-XC-3′, 5′-XT-3′, and 5′-XY-3′ sequences (X-AFB_1−FAPY; Y = 7-deaza-dG) (Chart 1) have been constructed, in which the 3′-neighbor base with respect to the adducted guanine has been changed from adenine to thymine, cytosine, and 7-deaza-dG. NMR analyses demonstrate that the equilibrium between *E* and *Z* isomers of the formamide moiety is controlled by major groove hydrogen bonding interactions. When the 3′ neighbor is adenine, the *E* isomer is favored. A mixture of *E* and *Z* isomers coexists when the 3′ neighbor is cytosine. The major isomer is the *E* isomer. In contrast, when the 3′ neighbor is either thymine or 7-deaza-dG, the *Z* isomer predominates. Structures of each of these duplexes have been refined from NMR data using molecular dynamics calculations restrained by NOE distances.

Chart 1. Four Oligodeoxynucleotide Duplexes Used in This Study[a]

A	5′-CTAAXATTCA-3′ 3′-GATTCTAAGT-5′
B	5′-CTAAXTTTCA-3′ 3′-GATTCAAAGT-5′
C	5′-CTAAXCTTCA-3′ 3′-GATTCGAAGT-5′
D	5′-CTAAXYTTCA-3′ 3′-GATTCCAAGT-5′

[a](A) The 5′-XA-3′ duplex. (B) The 5′-XT-3′ duplex. (C) The 5′-XC-3′ duplex. (D) The 5′-XY-3′ duplex. In all cases, X = AFB_1−FAPY; Y = 7-deaza-dG. In each instance, the 3′-neighbor base pair is shown in red.

MATERIALS AND METHODS

Materials. Unadducted oligodeoxynucleotides were purchased from the Midland Certified Reagent Co. (Midland, TX). AFB_1 was purchased from Aldrich Chemical Co. (Milwaukee, WI). AFB_1-*exo*-8,9-epoxide was prepared by oxidizing AFB_1 in the presence of dimethyldioxirane,[61−63] as described.[30]

Caution: *Crystalline AFB_1 is hazardous due to its electrostatic nature and should be handled using appropriate containment procedures and respiratory mask to prevent inhalation. AFB_1 can be destroyed by treatment with NaOCl. It should be assumed that AFB_1-exo-8,9-epoxide is toxic and carcinogenic. Manipulations should be carried out in a well-ventilated hood with suitable containment procedures.*

Sample Preparation. The oligodeoxynucleotide 5′-d-(CTAAGATTCA)-3′, containing the targeted *N*7-dG alkylation site (underlined) was annealed with 5′-d(ATCTT)-3′ to form a partially double-stranded scaffold in 200 μL of 100 mM Na_2HPO_4 (pH 6.5). AFB_1-*exo*-8,9-epoxide was added in 200 μL of CH_2Cl_2. The biphasic mixture was stirred for 15 min at 5 °C. The aqueous phase was dissolved in 100 mM Na_2CO_3 (pH 10) for 2 h at room temperature to form the AFB_1−FAPY adduct. The oligodeoxynucleotide containing the AFB_1−FAPY adduct 5′-d(CTAAXATTCA)-3′ (X = AFB_1−FAPY) was recovered from the aqueous phase using reverse-phase HPLC (Gemini C18 250 mm × 10 mm column, Phenomenix, Inc., Torrance, CA) at a flow rate of 2 mL/min, with a linear 30 min gradient of 5−30% CH_3CN in 0.1 M ammonium formate (pH 6.5). The eluent was monitored by UV absorbance at 260 and 360 nm. The adducted

DOI: 10.1021/tx5003832
Chem. Res. Toxicol. 2015, 28, 225−237

oligodexoynucleotide was lyophilized and characterized by MALDI-TOF mass spectrometry. The oligodeoxynucleotides 5′-d(CTAAXCTTCA)-3′, 5′-d(CTAAXTTTCA)-3′, and 5′-d(CTAAXYTTCA)-3′ (Y = 7-deazaG) were synthesized and characterized using the same procedures. Each purified AFB_1–FAPY modified oligodeoxynucleotide was annealed at room temperature with the complementary strand in buffer consisting of 10 mM NaH_2PO_4, 0.1 M NaCl, and 50 μM Na_2EDTA (pH 7.0), and the annealed duplex oligodeoxynucleotide was eluted from DNA grade Biogel hydroxylapatite using a gradient of 10–200 mM NaH_2PO_4 (pH 7.0). The modified duplexes were desalted by gel filtration chromatography over Sephadex G-25.

Thermal Melting Experiments. The melting temperatures were measured in 10 mM Na_2HPO_4, 0.1 M NaCl, and 50 μM Na_2EDTA (pH 7.0). The strand concentration was 1.6 μM. The temperature was increased at a rate of 1 °C/min from 10 to 80 °C. Absorbance was measured at 260 nm on a Varian Cary 4E spectrometer. The melting points (T_m values) of the unmodified and modified oligodeoxynucleotides were obtained by determining the inflection points of the absorbance vs temperature curves from the first-order derivatives.

NMR. Spectra were recorded at ^1H frequencies of 600, 800, and 900 MHz using cryogenic probes (Bruker Biospin, Inc., Billerica, MA). Samples were prepared in D_2O, containing 0.1 M NaCl, 10 mM NaH_2PO_4, and 50 μM Na_2EDTA (pH 7.0). The program TOPSPIN (Bruker Biospin, Inc., Billerica, MA) was used for data collection and processing. Chemical shifts were referenced to the chemical shift of the water resonance at the corresponding temperature, with respect to 4,4-dimethyl-4-silapentane-1-sulfonic acid (DSS). HMQC spectra[64,65] were recorded with 96 real data in the t_1 dimension and 1024 real data in the t_2 dimension. COSY and NOESY spectra were recorded with 512 real data in the t_1 dimension and 2048 real data in the t_2 dimension. In the NOESY experiment for exchangeable protons, the samples were prepared in 9:1 H_2O:D_2O and the water signal was suppressed by using the WATERGATE pulse sequence.[66] Resonance assignment and peak integration were performed using the program SPARKY.[67]

Experimental Restraints. Footprints were drawn around the NOE cross-peaks obtained at NOESY mixing times of 150, 200, and 250 ms using the program SPARKY. Cross-peak intensities were determined by volume integrations. The intensities of the cross-peaks were combined with the intensities generated from complete relaxation matrix analysis of a starting DNA structure to generate a hybrid intensity matrix.[68,69] The program MARDIGRAS,[70−72] using the RANDMARDI[72,73] algorithm, was used to refine the hybrid matrix by iteration between the calculated and experimental NOE intensities. The calculations were initiated using isotropic correlation times of 2, 3, and 4 ns. Analysis of this data yielded experimental distance restraints used in molecular dynamics calculations.

Molecular Dynamics Calculations. Restrained molecular dynamics (rMD) calculations for the oligodeoxynucleotide duplexes utilized a simulated annealing approach.[74] The AFB_1–FAPY modified oligonucleotides were constructed using the BUILDER module of INSIGHT II (Accelrys, Inc., San Diego, CA). The partial charges on the AFB_1–FAPY nucleotide were obtained from density function theory (DFT) calculations using a neutral total charge, utilizing the B3LYP/6-31G* basis set and the program GAUSSIAN.[75] To obtain the starting structures used for rMD calculations, the AFB_1 FAPY-modified duplex was energy minimized using 200 iterations with the conjugate gradients algorithm. The rMD calculations were conducted with AMBER[76] using the parm99[77] force field. The generalized Born (GB)[78] model with parameters developed by Tsui and Case[79] was used for implicit water simulation. The program CORMA[68,69] was utilized to calculate the NOE intensities from the structures emergent from rMD calculations. Molecular dynamics simulations in explicit water were performed using the AMBER force field. The average structure converged from the series of simulated annealing rMD calculations was used as the starting structure. This was placed in an truncated octahedral TIP3P water box with periodic boundaries at a distance of 8.0 Å from the solute.[80] The necessary Na^+ ions were added to neutralize the duplex using restraints having a lower bound of 3.0 Å and an upper bound of 8.0 Å. The system was subjected to 1000 iterations of potential energy minimization using steepest descents. The solvent was brought to thermal equilibrium by a rMD simulation at constant volume for 10000 iterations with an integrator time of 1 fs, at 300 K. The experimental distance and torsion angle restraints and empirical restraints were increased linearly during the heating. rMD calculations were performed at constant pressure for 1 ns with an integrator time of 1 fs. Bond lengths involving hydrogens were fixed with the SHAKE algorithm.[81] The particle mesh Ewald (PME) method was used to approximate nonbonded interactions.[82,83] The cutoff radius for nonbonded interactions was 8.0 Å. The PTRAJ program[76] from the AMBER package was used to analyze the rMD trajectories.

RESULTS

AFB_1–FAPY Modified Duplexes. The 10-mers 5′-d(CTAAGATTCA)-3′, 5′-d(CTAAGCTTCA)-3′, 5′-d(CTAAGTTTCA)-3′, and 5′-d(CTAAGYTTCA)-3′ were designed to contain a single guanine, the targeted *N*7-dG alkylation site (underlined). These were individually annealed with 5-mers, 5′-d(ATCTT)-3′, 5′-d(AACTT)-3′, containing a C:A mismatch, 5′-d(AACTT)-3′, or 5′-d(ACCTT)-3′, respectively, to form double-stranded scaffolds extending two base pairs in either direction from the targeted *N*7-dG alkylation site. The scaffold facilitated the reaction with AFB_1-*exo*-epoxide, by allowing intercalation above the 5′-face of the targeted guanine, and directing alkylation at the *N*7-dG position.[37,38] The resulting 10-mers containing *trans*-8,9-dihydro-8-(*N*7-guanyl)-9-hudroxy-AFB_1 adducts[36] were separated from the scaffolds using reverse-phase HPLC. Under basic conditions, over a period of several hours, the 10-mers spontaneously rearranged to the corresponding AFB_1–FAPY adducts.[39−41] The utilization of 7-deaza-dG in the 5′-XY-3′ sequence directed the alkylation to the single dG; it also facilitated the subsequent isolation of the AFB_1–FAPY modified oligodeoxynucleotide using reverse-phase HPLC. The 7-deaza-dG:C base pair was not anticipated to disrupt the helical structure of the duplex.[84] The 10-mers containing the AFB_1–FAPY adducts were characterized by MALDI-TOF mass spectrometry: for 5′-XA-3′, calcd 3357.1, found 3356.5; for 5′-XC-3′, calcd 3333.1, found 3333.2; for 5′-XT-3′, calcd 3348.1, found 3348.0; for 5′-XY-3′, calcd 3372.1, found 3372.8.

NMR of the AFB_1–FAPY Adducts. *a. AFB_1 Moiety.* For each of the four duplexes, one set of resonances of the X^5 AFB_1 moiety was observed. Figure 1 shows the data for the 5′-XC-3′ duplex. Figures S1, S2, and S3 in the Supporting Information show the corresponding spectra for the 5′-XA-3′, 5′-XT-3′, and 5′-XY-3′ duplexes. The AFB_1 H5, H6a, H8, H9, H9a, and $-OCH_3$ resonances were assigned similar to previous studies, consistent with the notion that in each instance, the AFB_1 moiety was intercalated above the 5′-face of the modified guanine and the each adduct maintained a similar R_a axial conformation for the C5–N^5 bond linking the pyrimidine ring to the formamido nitrogen.[41,56,85] The assignments of the AFB_1 protons are tabulated in Tables S1–S4 of the Supporting Information.

b. AFB_1–FAPY Formyl Group. A series of HMQC spectra[64,65] allowed the characterization of the *E*:*Z* equilibrium of the AFB_1–FAPY formyl group in the 5′-XA-3′, 5′-XC-3′, 5′-XT-3′, and 5′-XY-3′ duplexes (Figure 2). For the 5′-XA-3′ duplex, the carbonyl ^{13}C resonance was observed at 171 ppm, coupled to a proton resonance at 8.43 ppm. This resonance was assigned to the *E* geometrical isomer of the formyl group. For the 5′-XC-3′ duplex, two cross-peaks were observed in this

DOI: 10.1021/tx5003832
Chem. Res. Toxicol. 2015, 28, 225−237

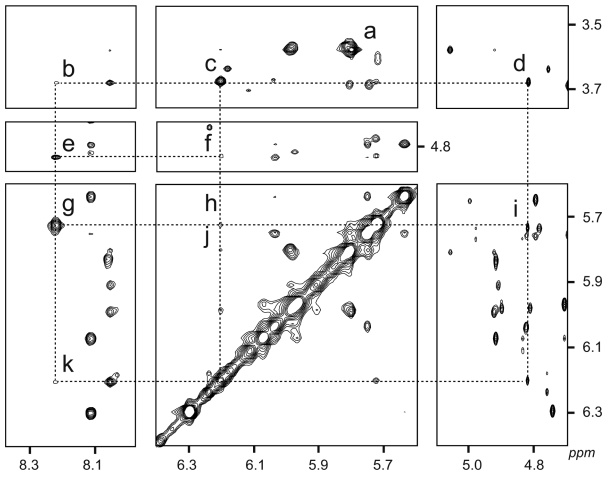

Figure 1. NOESY spectrum showing the assignments of the AFB_1 protons of the 5′-XC-3′ duplex. The cross peaks are assigned as (a) X^5 AFB_1 OCH_3 → X^5 AFB_1 H5; (b) X^5 AFB_1 H9a → X^5 AFB_1 CHO; (c) X^5 AFB_1 H9a → X^5 AFB_1 H6a; (d) X^5 AFB_1 H9a → X^5 AFB_1 H9; (e) X^5 AFB_1 H9 → X^5 AFB_1 CHO; (f) X^5 AFB_1 H9 → X^5 AFB_1 H6a; (g) X^5 AFB_1 H8 → X^5 AFB_1 CHO, (h) X^5 AFB_1 H8 → X^5 AFB_1 H6a, (i) X^5 AFB_1 H8 → X^5 AFB_1 H9, (j) X^5 AFB_1 H5 → X^5 AFB_1 H6a, (k) X^5 AFB_1 H6a → X^5 AFB_1 CHO. The 900 MHz spectrum with a mixing time of 250 ms was collected at 283 K. Corresponding spectra for the 5′-XA-3′, 5′-XT-3′, and 5′-XY-3′ duplexes may be found in Figures S1, S2, and S3 of the Supporting Information.

region of the HMQC spectrum, suggesting that for this duplex, two species were present in equilibrium. One ^{13}C carbonyl resonance at 167 ppm was coupled to a proton resonance at 8.33 ppm. The other ^{13}C carbonyl resonance at 168 ppm was coupled to a proton resonance at 7.47 ppm, assigned as the *Z* isomer of the formyl group. For the 5′-XT-3′ duplex, the carbonyl ^{13}C resonance was observed at 168 ppm, coupled to a proton resonance at 7.71 ppm. For the 5′-XY-3′ duplex, the carbonyl ^{13}C resonance was observed at 169 ppm, coupled to a proton resonance at 7.71 ppm. For each of the four duplexes, the assignments of the formyl proton resonances were supported by NOEs to the deoxyribose H1′ and AFB_1 H6a protons. Additionally, different NOEs were observed between the formyl protons and AFB_1 H8. For the 5′-XA-3′ and the major isomer of the 5′-XC-3′ duplexes, strong NOEs were observed between the X^5 formyl protons and the AFB_1 H8 proton, which were observed at δ 8.3 ppm and δ 5.7 ppm, respectively. For the 5′-XT-3′ and 5′-XY-3′ duplexes, weak NOEs were observed between the X^5 formyl protons and the AFB_1 H8 protons, which were observed at δ 7.7 ppm and δ 6.1 ppm, respectively.

c. Anomeric Configurations. NMR spectra of the nonexchangeable protons of the AFB_1–FAPY modified 5′-XA-3′, 5′-XC-3′, 5′-XT-3′, and 5′-XY-3′ duplexes were assigned using the sequential NOE connectivity of the base proton H6 or H8 dipolar couplings with H1′ deoxyribose protons.[86,87] For each of the duplexes, the deoxyribose spin systems were assigned from the assignments of the H1′ protons. The assignments of the deoxyribose H2′ and H2″ resonances were determined from the relative cross peak intensities in the NOESY spectrum between the H2′ and H2″ resonances and the H3′ resonances. These measurements were obtained at a NOE mixing time of 60 ms, which minimized spin diffusion. The anomeric configurations at X^5 C1′ were determined by analyzing the NOEs between the H2′ and H2″ protons and the

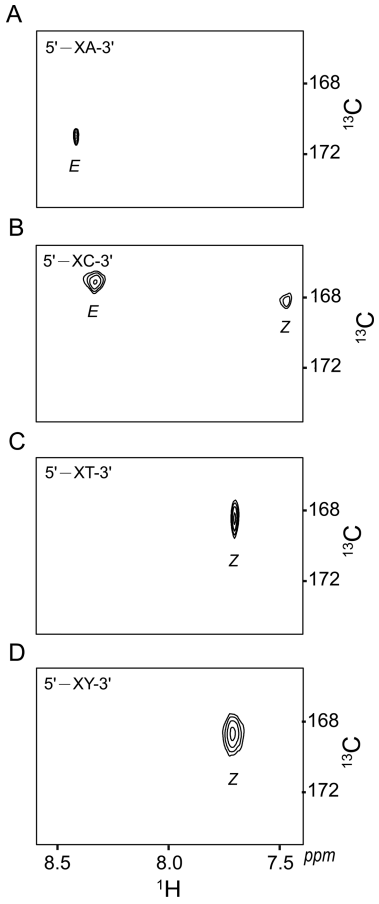

Figure 2. NMR analysis of the formyl group proton resonances for the four AFB_1–FAPY modified duplexes. The spectra show cross-peaks between the carbonyl ^{13}C resonance and the aldhyde proton resonances, for each of the four sequences. (A) The 5′-XA-3′ duplex. (B) The 5′-XC-3′ duplex. (C) The 5′-XT-3′ duplex. (D) The 5′-XY-3′ duplex. The HMQC spectra were collected at 283 K at a ^1H frequency of 600 MHz.

H1′ protons. Figure 3 shows the results for the *E* and *Z* geometrical isomers of 5′-XC-3′duplex. In each instance, the intensity of the X^5 H1′ to X^5 H2′ NOE was less than the X^5 H1′ to X^5 H2″ NOE, confirming the β configurations of the glycosyl bonds. Figures S4 and S5 of the Supporting Information show the corresponding data for the 5′-XA-3′- and 5′-XT-3′-duplexes.

d. Watson–Crick Base Pairing. For each of the 5′-XA-3′, 5′-XC-3′, 5′-XT-3′, and 5′-XY-3′ duplexes, the resonances of the nucleobase imino protons were assigned on the basis of sequential connectivity between adjacent base pairs in NOESY spectra. These assignments were supported by NOEs to the amino protons of Watson–Crick base pairs.[88] In each duplex, there was an interruption of the sequential imino-to-imino proton NOEs between the T^{17} N3H proton at base pair A^4:T^{17} and the X^5 N1H proton at base pair X^5:C^{16}, consistent with the 5′-intercalation of the AFB_1 moiety. In each duplex, at the X^5:T^{16} base pair, the observation of strong interstrand cross peaks from X^5 N1H to the C^{16} N^4 H1 and C^{16} N^4 H2 amino protons indicated that Watson–Crick hydrogen bonding between X^5 and C^{16} was intact (Figure 4). For the X^5 N1H imino proton in the 5′-XC-3′ duplex, two sets of resonances were observed at 278 K. The ratio between them was 1:2.8. Compared to the unmodified duplex, the C^6 N^4 H1 non-

DOI: 10.1021/tx5003832
Chem. Res. Toxicol. 2015, 28, 225–237

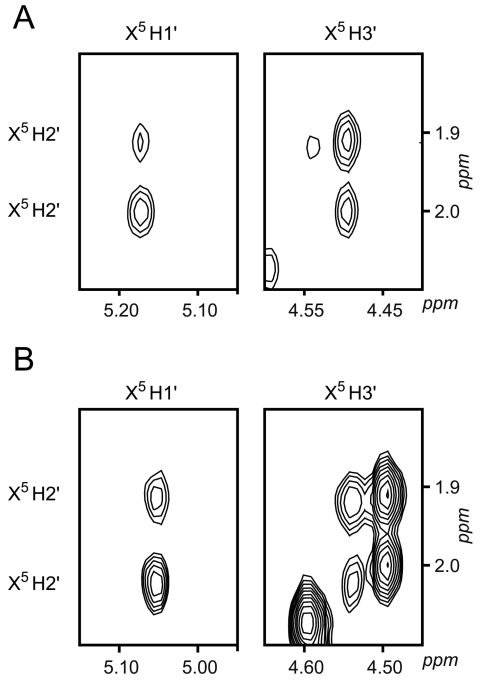

Figure 3. Comparison of NOE intensities for the cross-peaks arising between the X^5 H1′ and H3′ deoxyribose protons to the X^5 H2′ and H2″ deoxyribose protons for the *E* and *Z* geometrical isomers of the 5′-XC-3′ duplex. (A) The *E* isomer. (B) The *Z* isomer. The 900 MHz NOESY spectrum with a mixing time of 60 ms was collected at 283 K. Corresponding spectra of the 5′-XA-3′ and 5′-XT-3′ duplexes may be found in Figures S4 and S5 of the Supporting Information.

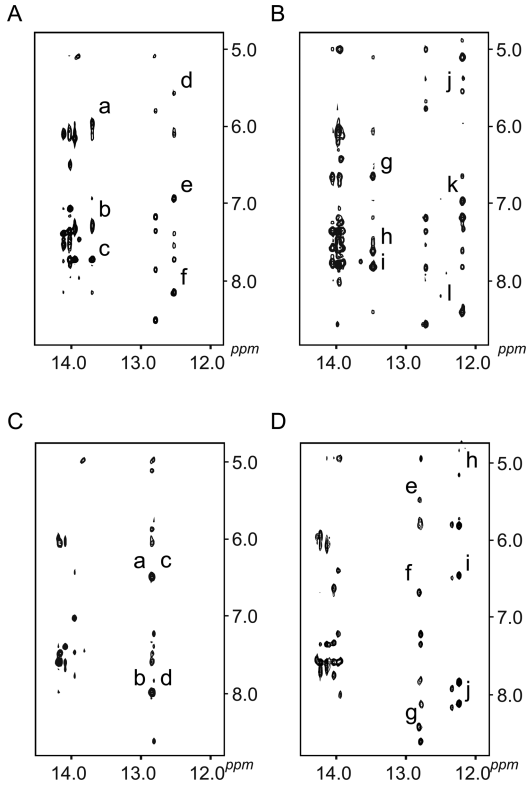

Figure 4. Comparison of the A^6 N^6 H1 and N^6 H2 amino proton resonances of the unmodified 5′-GA-3′ duplex with those of the 5′-XA-3′ duplex. (A) The 5′-GA-3′ duplex. The cross peaks are assigned as (a) A^6 N^6 H1 → T^{15} N3H; (b) A^6 N^6 H2 → T^{15} N3H; (c) A^6 H2 → T^{15} N3H; (d) C^{16} H5 → G^5 N1H; (e) C^{16} N^4 H1 → G^5 N1H; (f) C^{16} N^4 H2 → G^5 N1H. (B) 5′-XA-3′ duplex. The cross-peaks are assigned as (g) A^6 N^6 H1 → T^{15} N3H; (h) A^6 N^6 H2 → T^{15} N3H; (i) A^6 H2 → T^{15} N3H; (j) C^{16} H5 → X^5 N1H; (k) C^{16} N^4 H1 → X^5 N1H; (l) C^{16} N^4 H2 → X^5 N1H. Comparison of the C^6 N^4 H1 and N^4H2 amino proton resonances of the unmodified 5′-GC-3′ duplex with those of the 5′-XC-3′ duplex. (C) Unmodified 5′-GC-3′ duplex. The cross-peaks are assigned as (a) C^{16} N^4 H1 → G^5 N1H; (b) C^{16} N^4 H2 → G^5 N1H; (c) C^6 N^4 H1 → G^{15} N1H; (d) C^6 N^4 H2 → G^{15} N1H. (D) 5′-XC-3′ duplex. The cross-peaks are assigned as (e) C^6 H5 → G^{15} N1H; (f) C^6 N^4 H1 → G^{15} N1H; (g) C^6 N^4 H2 → G^{15} N1H; (h) C^{16} H5 → X^5 N1H; (i) C^{16} N^4 H1 → X^5 N1H; (j) C^{16} N^4 H2 → X^5 N1H. The NOESY spectra were collected at 800 MHz with a mixing time of 250 ms. The temperature was 278 K.

hydrogen bonded exocyclic amine proton shifted downfield 0.21 ppm at 278 K (Figure 4). The assignments of the exchangeable protons are tabulated in Tables S5−S8 of the Supporting Information.

e. DNA Duplex Structure. For each of the 5′-XA-3′, 5′-XC-3′, 5′-XT-3′, and 5′-XY-3′ duplexes, in the modified strand, the sequential NOE connectivity between nucleobase purine H8 or pyrimidine H6 protons and deoxyribose H1′ protons was observed from C^1 to A^4. In each instance, the sequential connectivity exhibited an interruption between A^4 H1′ and X^5 due to the loss of the guanine H8 proton because of the opening of the guanine imidazole ring (Figure 5). The connectivity resumed starting from an intranucleotide NOE between X^5 H1′ and the formyl proton of the FAPY base and continued to the 3′-terminus. For the complementary strand, in all instances, an interruption of the sequential NOEs was observed between C^{16} H1′ and T^{17} H8. For the 5′-XC-3′ duplex, two sets of resonances for several protons were observed for the base pairs X^5:C^{16}, C^6:G^{15}, and T^7:A^{14}, in both COSY and NOESY experiments, indicating the existence of two species. The assignments of the nonexchangeable protons are tabulated in Tables S9−S12 of the Supporting Information.

Thermal Stabilities of the Modified Duplexes. For the 5′-GA-3′, 5′-GC-3′, 5′-GT-3′, and 5′-GY-3′ unmodified duplexes, the T_m values, as monitored by UV absorbance at 260 nm, were 31, 37, 32, and 35 °C, respectively. The higher values of T_m for the 5′-GC-3′ and 5′-GY-3′ duplexes were attributed to the presence of the 3′-neighbor C:G or 7-deaza-dG:C base pairs vs 3′-neighbor A:T or T:A base pairs, respectively. As anticipated,[41,56,85] the presence of the AFB_1−FAPY adducts increased the thermal stabilities of each of the four duplexes. The melting points for the 5′-XA-3′, 5′-XC-3′, 5′-XT-3′, and 5′-XY-3′ duplexes were 41, 45, 41, and 45 °C, respectively. The higher values of T_m for the 5′-XC-3′ and 5′-XY-3′ duplexes were also attributed to the presence of the 3′-neighbor C:G or 7-deaza-dG:C base pairs, respectively.

The thermal melting of the 5′-XA-3′, 5′-XC-3′, 5′-XT-3′, and 5′-XY-3′ duplexes was also examined by monitoring NMR spectra of the imino protons as a function of temperature; the imino proton resonances were assigned using standard methods.[88] For each duplex, at the X^5:C^{16} base pair the X^5 N1H imino proton resonance and the 5′-neighbor A^4:T^{17} base pair T^{17} N3H imino proton resonance were observed at 40 °C (Figure 6). Increased stabilization of the 3′-neighbor base pairs was also observed. For the 5′-XA-3′ duplex the T^{15} N3H imino proton resonance was observed. For the 5′-XC-3′ duplex, the G^{15} N1H imino proton resonance was observed. At 308 K, the ratio between the two isomers changed to 1:2.2 (Figure 6). This was also observed in COSY experiments at both temperatures. The additional imino resonances at 308 K were

DOI: 10.1021/tx5003832
Chem. Res. Toxicol. 2015, 28, 225−237

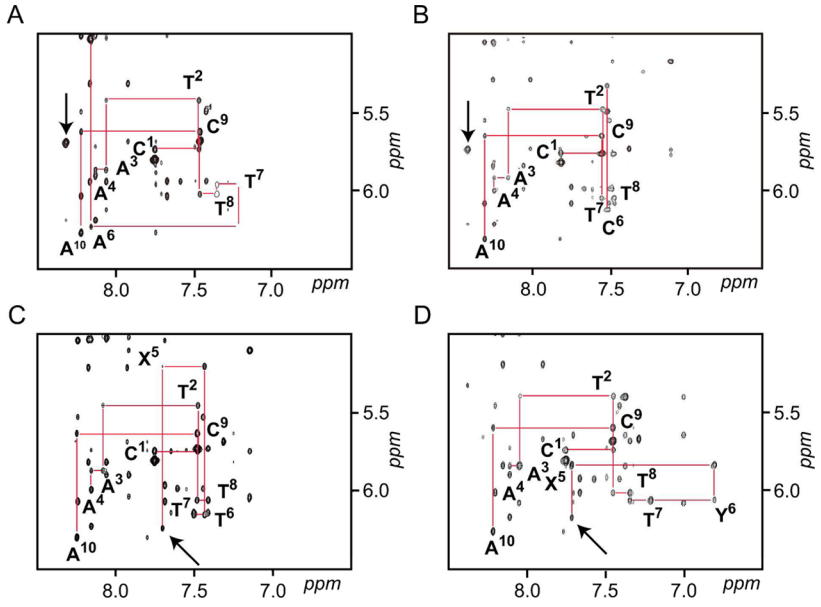

Figure 5. Sequential NOE connectivity of base H8 or H6 protons with deoxyribose H1′ protons for the four AFB_1−FAPY modified duplexes. (A) The 5′-XA-3′ duplex. (B) The 5′-XC-3′ duplex. (C) The 5′-XT-3′ duplex. (D) The 5′-XY-3′ duplex. X = AFB_1−FAPY, Y = 7-deaza-dG. The arrows indicate the NOEs between the formyl protons and the AFB_1 H8 protons. The 900 MHz NOESY spectra with a mixing time of 250 ms were collected at 283 K.

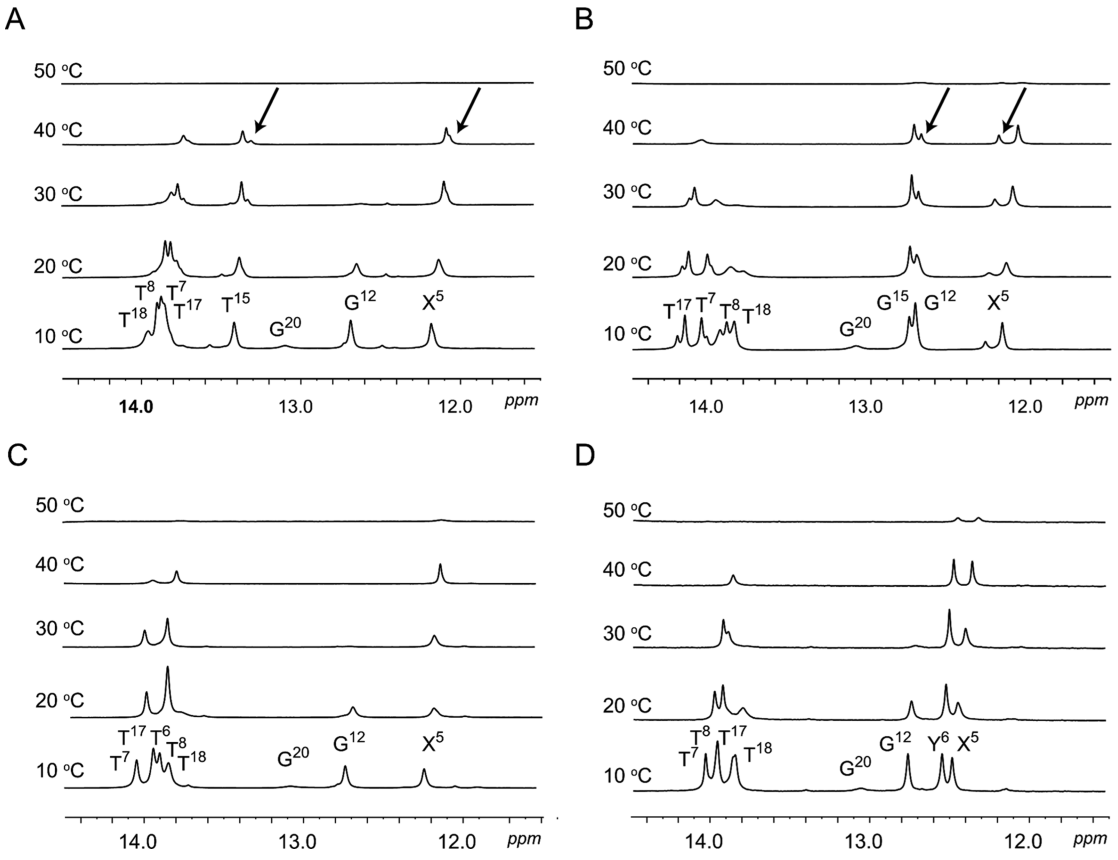

Figure 6. NMR spectra showing the Watson−Crick base paired imino proton region for the four AFB_1−FAPY modified duplexes as a function of temperature. (A) The 5′-XA-3′ duplex. (B) The 5′-XC-3′ duplex. (C) The 5′-XT-3′ duplex. (D) The 5′-XY-3′ duplex. The arrows indicate imino proton resonances assigned to the *Z* geometrical isomers in equilibrium with the *E* isomers for the 5′-XA-3′ and 5′-XC-3′ duplexes. X = AFB_1−FAPY, Y = 7-deaza-dG. The spectra were collected at a ^{1}H frequency of 800 MHz.

also observed for the G^{15} N1H resonance (Figure 6). For the 5′-XY-3′ duplex, the Y^6 N1H imino proton resonance was observed. For the 5′-XY-3′ duplex, a single resonance was observed at both 278 and 308 K for the X^5 N1H imino proton (Figure 6). For the 5′-XC-3′ duplex, the presence of two species in equilibrium was evident, with doubling of the imino

DOI: 10.1021/tx5003832
Chem. Res. Toxicol. 2015, 28, 225−237

proton resonances being observed for the X^5:C^{16} and 3′-neighboring C^6:G^{15} base pairs. The imino proton resonance for the 5′-neighbor A^4:T^{17} base pair exhibited line broadening. The ratio of the two species was approximately 3:1 at 10 °C, decreasing to 2:1 at 40 °C. Both species exhibited similar overall T_m values.

Structural Refinement of the Modified Duplexes. *a. NOEs Between AFB$_1$ and DNA.* For each of the 5′-XA-3′, 5′-XC-3′, 5′-XT-3′, and 5′-XY-3′ duplexes, the protons of the two AFB$_1$-fused furan rings showed NOEs to major groove and imino protons of the DNA; most of these were to the 5′ neighboring base-pair A^4:T^{17}. Thus, H6a and H9a, which are located on the same face of the AFB$_1$ moiety, both exhibited NOEs to A^4 H8. A weaker NOE was observed for AFB$_1$ H9. The AFB$_1$ H5 and $-OCH_3$ protons exhibited NOEs with minor groove and imino DNA protons. These were primarily to base A^4:T^{17} in the 5′ direction and to the modified nucleotide X^5. These included NOEs between AFB$_1$ $-OCH_3$ and A^4 H1′, A^4 H2′, A^4 H2″, A^4 H2, T^{17} N3H, X^5 H1′, and X^5 N1H. The cyclopentenone ring H2α and H2β produced NOEs with C^{16} H1′, H2′, and H2″, and T^{17} H1′, and H3′ of the complementary strand.

A series of rMD calculations, using a simulated annealing protocol, were performed from initial A- and B-form DNA starting structures for each of the AFB$_1$–FAPY modified duplexes. For the 5′-XC-3′ duplex, only the structure of the *E* isomer was refined; the *Z* isomer did not exhibit sufficient NOE cross-peaks to allow structural refinement. Emergent structures, five each from A- and B-DNA starting structures, with lowest energies, were obtained for each duplex and subjected to potential energy minimization. For each duplex, all structures converged as indicated by pairwise rmsd comparisons (Table 1, and Figures S6, S7, S8, and S9 in the Supporting Information). The accuracies of the emergent structures were evaluated by comparison of theoretical NOE intensities calculated by CORMA[70] for the refined structure to the experimental NOE intensities to yield sixth root residuals (R_1^x).[69] The R_1^x values for overall residuals, as well as the residuals for intra- or internucleotide NOEs, were consistently less than 0.1 (Table 1) and for each nucleotide were less than 0.15, suggesting that the refined structures for each duplex were in good agreement with the NOESY data. Figures S10, S11, S12, and S13 in the Supporting Information show the R_1^x values for individual nucleotides.

Table 1. Distribution of Restraints Applied to Structural Refinements and Statistical Analyses for the 5′-XA-3′, 5′-XC-3′, 5′-XT-3′, and 5′-XY-3′ Duplexes

	5′-XT-3′	5′-XY-3′	5′-XA-3′	5′-XC-3′
experimental NOE distance restraints	244	264	256	250
intranucleotide NOE restraints	152	161	160	159
internucleotide NOE restraints	92	103	96	91
NOEs of FAPY	41	39	34	34
empirical base pairing restraints	40	40	40	40
empirical backbone torsion restraints	50	50	50	50
empirical pseudorotation restraints	50	50	50	50
total restraints for rMD calculation	384	404	396	390
Structure Statistics				
NMR *R*-factor (*R**) ($\times 10^{-2}$)	6.88	8.28	8.09	7.47
intranucleotide NOEs	7.03	7.64	8.48	6.68
internucleotide NOEs	6.60	9.40	7.35	8.82
rmsd deviation of refined structures	0.48	0.63	0.48	0.50

Expanded views of the structures are shown in Figure 7. In each instance, the AFB$_1$ moiety intercalated above the 5′-face of the modified nucleotide X^5 and between base pairs A^4:T^{17} and X^5:C^{16}, causing the rise between these base pairs to increase to 7 Å. The adduct-induced unwinding was localized to the adducted base pairs X^5:C^{16} and their 5′- and 3′-neighbor base pairs A^4:T^{17} and A^6:T^{15}. The modified duplexes were each unwound approximately 15° at the adducted sites. For the 5′-XA-3′ duplex, the A^6 N^6 H1 non-Watson–Crick hydrogen bonded exocyclic amine proton was within hydrogen bonding distance of the X^5 formyl oxygen; this positioned the formamide moiety in the *E* configuration. For the 5′-XC-3′ duplex, only the structure of the *E* isomer was refined; the *Z* isomer did not exhibit sufficient NOE cross-peaks to allow structural refinement. The C^6 N^4 H1 non-Watson–Crick hydrogen bonded exocyclic amine proton was within hydrogen bonding distance of the X^5 formyl oxygen; this positioned the formamide in the *E* configuration. The structure of the 5′-XT-3′ duplex positioned the formamide in the *Z* configuration. The structure suggested that the X^5 formyl oxygen was within hydrogen bonding distance of the X^5 N9H exocyclic amine proton.

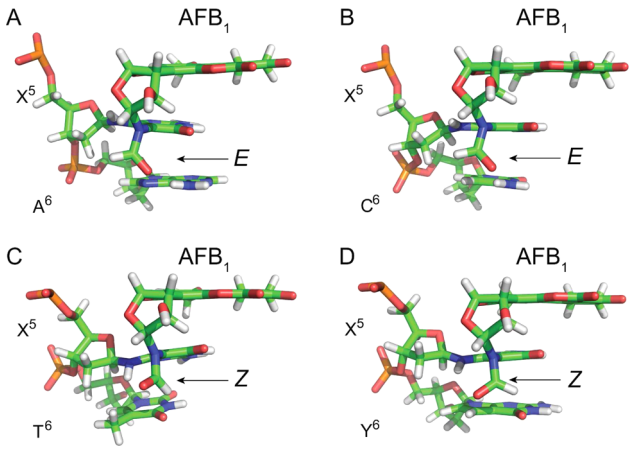

Figure 7. Refined structures of the four AFB$_1$–FAPY modified duplexes. (A) The 5′-XA-3′ duplex. (B) The 5′-XC-3′ duplex. (C) The 5′-XT-3′ duplex. (D) The 5′-XY-3′ duplex. X = AFB$_1$-β-FAPY, Y = 7-deaza-dG.

Molecular Dynamics Simulations. For each of the 5′-XA-3′, 5′-XC-3′, 5′-XT-3′, and 5′-XY-3′ duplexes, 1 ns of equilibrium rMD calculation was performed in explicit water at constant pressure at 300 K to examine the dynamics of the refined structure and to analyze hydrogen bond occupancies involving the formyl oxygen atom of the AFB$_1$–FAPY adduct. The 1 ns rMD trajectory was analyzed for occupancies of hydrogen bonding motifs. Hydrogen bond occupancies were calculated using a distance cutoff of 3.5 Å and an angle cutoff of 120°. Using these criteria, for the 5′-XA-3′ duplex, the hydrogen bond between the formyl oxygen and the A^6 N^6-dA exocyclic amino group was satisfied for >95% of the trajectory. Using the same criteria, for the *E* configuration of the 5′-XC-3′ duplex, this hydrogen bond was satisfied for 93% of the

DOI: 10.1021/tx5003832
Chem. Res. Toxicol. 2015, 28, 225–237

trajectory. In contrast, using these criteria, for the 5′-XT-3′, and 5′-XY-3′ duplexes the rMD trajectories in explicit solvent suggested that the X^5 formyl oxygen was within hydrogen bonding distance of the X^5 N9H exocyclic amine proton; this positioned the formamide in the *Z* configuration. This orientation was satisfied for approximately 75% of the trajectory for both the 5′-XT-3′, and 5′-XY-3′ duplexes.

Deposition of Structural Coordinates. The structural coordinates for the 5′-XA-3′ duplex, the *E* isomer of the 5′-XC-3′ duplex, the 5′-XT-3′ duplex, and the 5′-XY-3′ duplex have been deposited in the Protein Data Bank. PDB ID codes: 2MMF for the 5′-XA-3′ duplex, 2MMR for the *E* isomer of the 5′-XC-3′ duplex, 2MMQ for the 5′-XT-3′ duplex, and 2MMS for the 5′-XY-3′ duplex.

DISCUSSION

The structures of AFB_1–FAPY adducts in DNA[56−58] and in template:primer complexes with DNA damage bypass polymerases[89] are of interest due to their potential to equilibrate between α and β deoxyribose anomers, atropisomers of the C5–N^5 bond linking the pyrimidine ring to the formamide nitrogen, and geometrical isomers of the formamide moiety.[41] In duplex DNA, in differing sequence contexts, these equilibria are anticipated to modulate the biological processing and genotoxicity of AFB_1–FAPY adducts. The AFB_1–FAPY adduct[41,42] may be linked to site-specific G → T transversions in the tumor suppression gene p53[47−54] and *ras* proto-oncogenes.[55]

Sequence-Specific Hydrogen Bonding in DNA Modulates Geometrical Isomerism of the AFB_1–FAPY Formamide Group. In the 5′-XA-3′ duplex, the *E* configuration of the formamide group (Figure 2) allows formation of a hydrogen bond between the formyl oxygen of the AFB_1–FAPY adduct and the N^6-dA non-Watson–Crick hydrogen bonded exocyclic amino proton of the 3′-neighbor A^6 (Figure 7). Several features of the NMR spectrum provide evidence for the existence of this hydrogen bond, which had been predicted from studies by Mao et al.[56] and Brown et al.[58] The downfield chemical shifts of the formyl proton (Figure 2) and the A^6 non-Watson–Crick exocyclic amino proton (Figure 4) are consistent with the electronic deshielding of both protons. The appearance of an additional NMR resonance at 308 K, assigned to the *Z* configuration (Figure 6), suggests that the *Z* configuration is favored in the absence of a thermally stable DNA duplex, as is observed at the nucleoside level.[58] The slow interconversion of *E* and *Z* isomers (Figure 6) is consistent with a significant lifetime for this hydrogen bond on the NMR time scale. It suggests that the interconversion between the two configurations within the major groove is sterically hindered in duplex DNA. In support of this conclusion, the rMD trajectories calculated in the presence of explicit solvent over a 1 ns time period predict a significant occupancy of this hydrogen bond.

In the 5′-XC-3′ duplex, a mixture of *E* and *Z* isomers is observed (Figure 2). The intensity of the NOE between the formyl proton and AFB_1 H8 proton establishes the major isomer as the *E* configuration (Figure 5). This allows for the formation of a hydrogen bond between the formyl oxygen and the C^6 N^4-dC non-Watson–Crick amino proton (Figure 7). In the refined structure, the distance between the formyl oxygen and C^6 N^4 H1 is 2.7 Å, and the calculated angle O···H——N is 110° (Figure 7). As compared to the 5′-XA-3′ duplex, the C^6 N^4-dC non-Watson–Crick amino proton is less deshielded in the 5′-XC-3′ duplex (Figure 4). This suggests a weaker hydrogen bond, as compared to the 5′-XA-3′ duplex. The coexistence of α and β anomers is ruled out by comparison of the NOEs intensities between the X^5 H1′ to X^5 H2′ and H2″, which indicates that both *E* and *Z* geometrical isomers maintain the β configuration of the deoxyribose (Figure 3). Moreover, only one set of NMR resonances is observed for the X^5 AFB_1 moiety (Figure 1) and the coexistence of both α and β anomers would have been predicted to result in distinguishable subspectra for each isomer.[58] Similar to the 5-XA-3′ duplex, as the temperature is increased from 278 to 308 K, the equilibrium shifts toward the *Z* isomer (Figure 6). This again suggests that the *Z* configuration is favored in single-strand DNA,[58] but that in duplex DNA, the major groove hydrogen bonding favors the *E* configuration. As for the 5-XA-3′ duplex, slow interconversion of *E* and *Z* isomers (Figure 6) suggests a significant lifetime for this hydrogen bond and that interconversion between the two geometrical isomers within the major groove is hindered in duplex DNA. The rMD trajectories calculated in the presence of explicit solvent over a 1 ns time period are consistent with this conclusion and predict significant occupancy of this hydrogen bond.

In the 5′-XT-3′ and 5′-XY-3′ duplexes, there is no 3′-neighbor exocyclic amino proton in the major groove for either T or 7-deaza-dG, so a major groove hydrogen bond cannot form. Consequently, the formamide moiety favors the *Z* geometrical isomer (Figure 2), as is observed at the nucleoside level.[58] For both duplexes, the preference of the *Z* isomer is confirmed by the less intense NOE between the formyl proton and AFB_1 H8 proton, as compared to the 5′-XA-3′ duplex, indicating a greater distance between the two protons in the *Z* isomer (Figure 5). For the 5′-XT-3′ duplex, the refined structure predicts that the distance between the formyl oxygen and X^5 N9H is 3.1 Å, and the calculated angle O···H——N is 138° (Figure 7). For the 5′-XY-3′ duplex, the corresponding predicted distance is 2.7 Å and 147° (Figure 7). These results suggest that the *Z* isomer could be stabilized by a hydrogen bond between the formyl oxygen of the AFB_1–FAPY adduct and the X^5 N9H exocyclic amine proton. However, the rMD trajectories calculated in explicit solvent are equivocal. They suggest 76% and 81% occupancies for this hydrogen bond in the 5′-XT-3′ and 5′-XY-3′ duplexes, respectively. The observation of a single NMR resonance for the X^5 N1H imino proton at both 278 and 308 K for both the 5′-XT-3′ and 5′-XY-3′ duplexes (Figure 6) is consistent with the notion that the *Z* isomer is favored at all temperatures.[58] Likewise, a single resonance is observed for the imino protons of the 3′-neighbors, T^6 N3H and 7-deaza-dG^6 N1H in the 5′-XT-3′ and 5′-XY-3′ duplexes, respectively, at 308 K (Figure 6).

Structures of the AFB_1–FAPY Adducts. The significant structural differences between the four AFB_1–FAPY adducts studied here, under equilibrium conditions, are with regard to the geometrical isomerization of the formamide moiety in the major groove (Figure 7). For each of the four duplexes, only one set of NMR resonances is observed for the X^5 AFB_1 moiety (Figure 1), which indicates that the equilibrium between *E* and *Z* isomers induces a localized perturbation to the duplex. Spectroscopic differences between the *E* and *Z* isomers are confined to base pairs X^5:C^{16}, C^6:G^{15}, and T^7:A^{14}, and the modest chemical shift perturbations of corresponding nucleobase and deoxyribose H1′ protons of the *E* and *Z* isomers become smaller proceeding from the modified base pair X^5:C^{16} and proceeding in the 3′-direction toward base pairs C^6:G^{15},

DOI: 10.1021/tx5003832
Chem. Res. Toxicol. 2015, 28, 225−237

and T^7:A^{14} (Figure 5). The equilibria between α and β anomers[41] and the atropisomerism about the C5−N^5 bond[41] do not exhibit sequence dependence. For all four duplexes, the AFB_1 moiety intercalates above the 5′-face of the damaged base, the R_a axial conformation about the C5−N^5 bond is maintained, and the β anomer of the deoxyribose is favored, similar to studies of the β anomer of the AFB_1−FAPY adduct.[56,57] A study of the α anomer of the AFB_1−FAPY adduct[58] concluded that the AFB_1 moiety also intercalates on the 5′ face of the damaged base, also maintaining the R_a axial conformation about the C5−N^5 bond. However, perturbations of the ε and ζ backbone torsion angles were observed, and the base stacking of the duplex was perturbed, which correlates with the observation that the α anomer of the AFB_1−FAPY adduct blocks DNA replication.[42]

Thermodynamic Considerations. One notable feature of the β anomer of the AFB_1−FAPY adduct is its thermal stabilization of the DNA duplex.[56,57] It has been proposed that hydrogen bonding between the formyl oxygen of the AFB_1−FAPY adduct and the N^6 non-Watson−Crick hydrogen bonded exocyclic amino proton of the 3′-neighbor A^6 provides a potential contribution to this stabilization,[56,57] but the present results suggests that this is not the major contributing factor. Although in the 5′-XA-3′ and 5′-XT-3′ duplexes, the formamide is held in *E* vs *Z* isomers, the 5′-intercalation of the AFB_1 moiety stabilizes both 5′-XA-3′ and 5′-XT-3′ duplexes by a similar 10 °C increase in T_m, as compared to the unadducted duplexes. A similar increase in T_m is observed in the 5′-XY-3′ and 5′-XC-3′ duplexes. Therefore, it seems that the hydrogen bond between the AFB_1 formamide moiety and the 3′- neighbor base, an intrastrand hydrogen bond, does not contribute to the stability of the AFB_1−FAPY modified DNA duplex. Instead, the thermal stability of the β anomer of the AFB_1−FAPY adduct in duplex DNA is likely attributable to favorable base stacking interactions.[56,57]

Biological Implications. Sequence-dependent hydrogen bonding patterns in the DNA major groove modulate *E* vs *Z* geometrical isomerism of the formamide moiety of the AFB_1−FAPY adduct. The differential accommodation of these AFB_1−FAPY adducts within the active site may, in part, modulate lesion bypass. It will be of interest to determine if sequence-dependent structural perturbations, observed here for DNA duplexes in vitro and at equilibrium, are translated into differential outcomes during error-prone replication bypass of the AFB_1−FAPY adduct. Banerjee et al.[89] have obtained structural data for the error-prone bypass of the AFB_1−FAPY adduct by the *Sulfolobus solfataricus* P2 DNA polymerase IV (Dpo4) in the 5′-XA-3′ sequence context. The Dpo4 polymerase conducts error-prone replication past the AFB_1−FAPY adduct, including misinsertion of dATP, consistent with G → T transversions.[8,42−44] In the 5′-XA-3′ sequence, the structure of a ternary (Dpo4−DNA−dATP) AFB_1−FAPY adducted template reveals that the oxygen atom of the FAPY formyl group participates in a water-mediated hydrogen bond with polymerase residue Arg^{332}.[89] In this case, the AFB_1−FAPY formamide group exists as the *Z* geometrical isomer.[89] Thus, geometrical isomerism of the AFB_1−FAPY formamide group is modulated not only by DNA sequence but also by specific interactions within the active sites of specific error-prone bypass polymerases. It is also possible that geometrical isomerism of the AFB_1−FAPY formamide group modulates the recognition and repair of these adducts in a sequence-specific manner. FAPY-type adducts are often substrates for base excision repair (BER),[90] but the AFB_1−FAPY adduct is a substrate for nucleotide excision repair (NER) in bacterial,[91] yeast,[92] and mammalian cells.[93−95] These reports are consistent with the notion that NER targets bulky DNA lesions. On the other hand, the AFB_1−FAPY lesion thermally stabilizes the DNA duplex.[56,85] Such thermal stabilization has been associated with resistance to NER.[96,97] Additionally, the data suggest differences in damage recognition between bacterial and mammalian repair systems. Croy and Wogan[46] noted that the AFB_1−FAPY lesion is removed less efficiently in mammalian cells than is the initially formed AFB_1−*N*7-dG cationic adduct, whereas both lesions are repaired with equal efficiencies in bacteria. More recently, Alekseyov et al.[91] confirmed that in *Escherichia coli* AFB_1−FAPY lesions are efficiently repaired by NER. While Takahashi[98] had reported that XPA-deficient mice exhibited enhanced AFB_1-induced liver tumorigenesis, Mulder et al.[99] did not observe increased repair of AFB_1−FAPY adducts in lung or liver extracts of NER-compromised heterozygous p53 knockout mice and they also did not observe changes in XPA or XPB protein levels in the p53 knockout mice. Consequently, the precise factors modulating NER recognition and repair of AFB_1−FAPY lesions remain incompletely understood. There is precedent for the idea that sequence-specific differences in DNA adduct structure may modulate NER efficiencies. Geacintov, Broyde, and co-workers[100−102] have investigated the sequence dependence of NER and have noted the potential for sequence specific differences in steric factors involving the minor groove-aligned PAH adducts and nearby guanine amino groups; they conclude that the NER apparatus binds productively or unproductively to the damaged DNA duplex depending upon the structural and stereochemical properties of specific DNA adducts.[102] Thus, it will be of interest to examine DNA sequence modulation of NER for AFB_1−FAPY adducts.

■ ASSOCIATED CONTENT

Supporting Information

Assignments of AFB_1 proton resonances, 5′-XA-3′ duplex; assignments of AFB_1 proton resonances, 5′-XT-3′ duplex; assignments of AFB_1 proton resonances, 5′-XY-3′ duplex; assignments of AFB_1 proton resonances, 5′-XC-3′ duplex; assignments of exchangeable proton resonances, 5′-XA-3′ duplex; assignments of exchangeable proton resonances, 5′-XT-3′ duplex; assignments of exchangeable proton resonances, 5′-XY-3′ duplex; assignments of exchangeable proton resonances, *E* isomer, 5′-XC-3′ duplex; assignments of nonexchangeable proton resonances, 5′-XA-3′ duplex; assignments of nonexchangeable proton resonances, 5′-XT-3′ duplex; assignments of nonexchangeable proton resonances, 5′-XY-3′ duplex; assignments of nonexchangeable proton resonances, *E* isomer, 5′-XC-3′ duplex; NOESY spectrum showing the assignments of the AFB_1 protons of the 5′-XA-3′ duplex; NOESY spectrum showing the assignments of the AFB_1 protons of the 5′-XT-3′ duplex; NOESY spectrum showing the assignments of the AFB_1 protons of the 5′-XY-3′ duplex; NOE intensities for the deoxyribose protons of the 5′-XA-3′ duplex; NOE intensities for the deoxyribose protons of the 5′-XT-3′ duplex; superposition of five lowest energy structures emergent from the rMD calculations for the 5′-XA-3′ duplex, using a simulated annealing protocol; superposition of five lowest energy structures emergent from the rMD calculations for the *E* isomer of the 5′-XC-3′ duplex, using a simulated annealing protocol; superposition of five lowest energy structures emergent from the rMD calculations for the 5′-

DOI: 10.1021/tx5003832
Chem. Res. Toxicol. 2015, 28, 225−237

XT-3′ duplex, using a simulated annealing protocol; superposition of five lowest energy structures emergent from the rMD calculations for the 5′-XY-3′ duplex, using a simulated annealing protocol; sixth root residual R_1^x values per nucleotide, 5′-XA-3′ duplex, calculated using CORMA; sixth root residual R_1^x values per nucleotide, *E* Isomer, 5′-XC-3′ duplex, calculated using CORMA; sixth root residual R_1^x values per nucleotide, 5′-XT-3′ duplex, calculated using CORMA; sixth root residual R_1^x values per nucleotide, 5′-XY-3′ duplex, calculated using CORMA. This material is available free of charge via the Internet at http://pubs.acs.org.

Accession Codes

The structural coordinates for the 5′-XA-3′ duplex, the *E* isomer of the 5′-XC-3′ duplex, the 5′-XT-3′ duplex, and the 5′-XY-3′ duplex have been deposited in the Protein Data Bank. PDB ID codes: 2MMF for the 5′-XA-3′ duplex, 2MMR for the *E* isomer of the 5′-XC-3′ duplex, 2MMQ for the 5′-XT-3′ duplex, and 2MMS for the 5′-XY-3′ duplex.

AUTHOR INFORMATION

Corresponding Author

*E-mail: michael.p.stone@vanderbilt.edu.

Funding

This work was supported by NIH grant R01 CA-55678 (M.P.S.). The Vanderbilt University Center in Molecular Toxicology is supported by NIH grant P30 ES-00267. The Vanderbilt-Ingram Cancer Center is funded by NIH grant P30 CA-68485. Funding for NMR was supplied by NIH grants S10 RR-05805, S10 RR-025677, and NSF grant DBI 0922862, the latter funded by the American Recovery and Reinvestment Act of 2009 (Public Law 111-5).

Notes

The authors declare no competing financial interest.

ACKNOWLEDGMENTS

Vanderbilt University assisted with the purchase of NMR instrumentation. Portions of this work were presented by L.L. at the 246th National Meeting of the American Chemical Society, Division of Chemical Toxicology, September 8−12, 2013, Indianapolis, IN.

ABBREVIATIONS

AFB_1, aflatoxin B_1; AFB_1−FAPY, AFB_1−formamidopyrimidine adduct; AMBER, assisted model building with energy refinement; BER, base excision repair; CORMA, complete relaxation matrix analysis; COSY, correlated spectroscopy; dA, 2′-deoxyadenosine; dATP, deoxyadenosine triphosphate; DFT, density function theory; dG, 2′-deoxyguanosine; Dpo4, *Sulfolobus solfataricus* P2 DNA polymerase IV; DSS, 4,4-dimethyl-4-silapentane-1-sulfonic acid; EDTA, ethylenediaminetetraacetic acid; GB, generalized Born; HBV, hepatitis B virus; HCC, hepatocellular carcinomas; HMQC, heteronuclear multiple-quantum correlation; HPLC, high-performance liquid chromatography; MALDI-TOF, matrix assisted laser desorption ionization time-of-flight; MARDIGRAS, matrix analysis of relaxation for discerning the geometry of an aqueous structure; NER, nucleotide excision repair; NMR, nuclear magnetic resonance; NOE, nuclear Overhauser effect; NOESY, nuclear Overhauser effect spectroscopy; PAH, polycyclic aromatic hydrocarbon; PME, particle mesh Ewald; RANDMARDI, random error MARDIGRAS; rMD, restrained molecular dynamics; WATERGATE, water suppression by gradient tailored excitation

REFERENCES

(1) Busby Jr., W. F., and Wogan, G. N. (1984) Aflatoxins, in *Chemical Carcinogens*, ACS Monograph Series 173 (Searle, C. E., Ed.) pp 945−1136, American Chemical Society, Washington, DC.

(2) Smela, M. E., Currier, S. S., Bailey, E. A., and Essigmann, J. M. (2001) The chemistry and biology of aflatoxin B_1: from mutational spectrometry to carcinogenesis. *Carcinogenesis 22*, 535−545.

(3) Bennett, J. W., and Klich, M. (2003) Mycotoxins. *Clin. Microbiol. Rev. 16*, 497−516.

(4) Kensler, T. W., Roebuck, B. D., Wogan, G. N., and Groopman, J. D. (2011) Aflatoxin: A 50-Year Odyssey of Mechanistic and Translational Toxicology. *Toxicol. Sci. 120*, S28−S48.

(5) McCann, J., Spingarn, N. E., Koburi, J., and Ames, B. N. (1975) Detection of carcinogens as mutagens—bacterial tester strains with R-factor plasmids. *Proc. Natl. Acad. Sci. U. S. A. 72*, 979−983.

(6) Foster, P. L., Eisenstadt, E., and Miller, J. H. (1983) Base substitution mutations induced by metabolically activated aflatoxin B_1. *Proc. Natl. Acad. Sci. U. S. A. 80*, 2695−2698.

(7) Foster, P. L., Groopman, J. D., and Eisenstadt, E. (1988) Induction of base substitution mutations by aflatoxin B_1 is *MucAB* dependent in *Escherichia coli*. *J. Bacteriol. 170*, 3415−3420.

(8) Lin, Y. C., Li, L., Makarova, A. V., Burgers, P. M., Stone, M. P., and Lloyd, R. S. (2014) Molecular basis of aflatoxin-induced mutagenesis—role of the aflatoxin B_1-formamidopyrimidine adduct. *Carcinogenesis 35*, 1461−1468.

(9) Williams, D. E. (2012) The rainbow trout liver cancer model: response to environmental chemicals and studies on promotion and chemoprevention. *Comp. Biochem. Physiol., Part C: Toxicol. Pharmacol. 155*, 121−127.

(10) Cullen, J. M., Brown, D. L., Kissling, G. E., Foley, J. F., Rizzo, J., Marion, P. L., Parron, V. I., and French, J. E. (2009) Aflatoxin B_1 and/or hepatitis B virus induced tumor spectrum in a genetically engineered hepatitis B virus expression and Trp53 haploinsufficient mouse model system for hepatocarcinogenesis. *Toxicol. Pathol. 37*, 333−342.

(11) Woo, L. L., Egner, P. A., Belanger, C. L., Wattanawaraporn, R., Trudel, L. J., Croy, R. G., Groopman, J. D., Essigmann, J. M., Wogan, G. N., and Bouhenguel, J. T. (2011) Aflatoxin B_1−DNA adduct formation and mutagenicity in livers of neonatal male and female B6C3F1 mice. *Toxicol. Sci. 122*, 38−44.

(12) Jeannot, E., Boorman, G. A., Kosyk, O., Bradford, B. U., Shymoniak, S., Tumurbaatar, B., Weinman, S. A., Melnyk, S. B., Tryndyak, V., Pogribny, I. P., and Rusyn, I. (2012) Increased incidence of aflatoxin B_1-induced liver tumors in hepatitis virus C transgenic mice. *Int. J. Cancer 130*, 1347−1356.

(13) Wang, J. S., Huang, T., Su, J. J., Liang, F., Wei, Z. L., Liang, Y. Q., Luo, H. T., Kuang, S. Y., Qian, G. S., Sun, G. J., He, X., Kensler, T. W., and Groopman, J. D. (2001) Hepatocellular carcinoma and aflatoxin exposure in Zhuqing Village, Fusui County, People's Republic of China. *Cancer Epidemiol., Biomarkers Prev. 10*, 143−146.

(14) Egner, P. A., Wang, J. B., Zhu, Y. R., Jacobson, L. P., Ng, D., Munoz, A., Fahey, J. W., Chen, J. G., Chen, T. Y., Qian, G. S., Groopman, J. D., and Kensler, T. W. (2013) Prevention of liver cancer in Qidong, China: lessons from aflatoxin biomarker studies. *Prog. Chem. 25*, 1454−1461.

(15) Groopman, J. D., Kensler, T. W., and Wild, C. P. (2008) Protective interventions to prevent aflatoxin-induced carcinogenesis in developing countries. *Annu. Rev. Public Health 29*, 187−203.

(16) Gnonlonfin, G. J., Hell, K., Adjovi, Y., Fandohan, P., Koudande, D. O., Mensah, G. A., Sanni, A., and Brimer, L. (2013) A review on aflatoxin contamination and its implications in the developing world: a sub-Saharan African perspective. *Crit. Rev. Food Sci. Nutr. 53*, 349−365.

(17) Groopman, J. D., Cain, L. G., and Kensler, T. W. (1988) Aflatoxin exposure in human populations: measurements and relationship to cancer. *CRC Crit. Rev. Toxicol. 19*, 113−145.

DOI: 10.1021/tx5003832
Chem. Res. Toxicol. 2015, 28, 225−237

(18) Wogan, G. N., Kensler, T. W., and Groopman, J. D. (2012) Present and future directions of translational research on aflatoxin and hepatocellular carcinoma. A review. *Food Addit. Contam., Part A: Chem. Anal. Control Exposure Risk Assess. 29*, 249−257.
(19) Chen, J. G., Egner, P. A., Ng, D., Jacobson, L. P., Munoz, A., Zhu, Y. R., Qian, G. S., Wu, F., Yuan, J. M., Groopman, J. D., and Kensler, T. W. (2013) Reduced aflatoxin exposure presages decline in liver cancer mortality in an endemic region of China. *Cancer Prev. Res. 6*, 1038−1045.
(20) Groopman, J. D., Wang, J. S., and Scholl, P. (1996) Molecular biomarkers for aflatoxins: from adducts to gene mutations to human liver cancer. *Can. J. Physiol. Pharmacol. 74*, 203−209.
(21) McCoy, L. F., Scholl, P. F., Sutcliffe, A. E., Kieszak, S. M., Powers, C. D., Rogers, H. S., Gong, Y. Y., Groopman, J. D., Wild, C. P., and Schleicher, R. L. (2008) Human aflatoxin albumin adducts quantitatively compared by ELISA, HPLC with fluorescence detection, and HPLC with isotope dilution mass spectrometry. *Cancer Epidemiol., Biomarkers Prev. 17*, 1653−1657.
(22) Wang, J. S., Shen, X. N., He, X., Zhu, Y. R., Zhang, B. C., Wang, J. B., Qian, G. S., Kuang, S. Y., Zarba, A., Egner, P. A., Jacobson, L. P., Munoz, A., Helzlsouer, K. J., Groopman, J. D., and Kensler, T. W. (1999) Protective alterations in phase 1 and 2 metabolism of aflatoxin B_1 by oltipraz in residents of Qidong, People's Republic of China. *J. Natl. Cancer Inst. 91*, 347−354.
(23) Egner, P. A., Wang, J. B., Zhu, Y. R., Zhang, B. C., Wu, Y., Zhang, Q. N., Qian, G. S., Kuang, S. Y., Gange, S. J., Jacobson, L. P., Helzlsouer, K. J., Bailey, G. S., Groopman, J. D., and Kensler, T. W. (2001) Chlorophyllin intervention reduces aflatoxin−DNA adducts in individuals at high risk for liver cancer. *Proc. Natl. Acad. Sci. U. S. A. 98*, 14601−14606.
(24) Liby, K., Yore, M. M., Roebuck, B. D., Baumgartner, K. J., Honda, T., Sundararajan, C., Yoshizawa, H., Gribble, G. W., Williams, C. R., Risingsong, R., Royce, D. B., Dinkova-Kostova, A. T., Stephenson, K. K., Egner, P. A., Yates, M. S., Groopman, J. D., Kensler, T. W., and Sporn, M. B. (2008) A novel acetylenic tricyclic bis-(cyano enone) potently induces phase 2 cytoprotective pathways and blocks liver carcinogenesis induced by aflatoxin. *Cancer Res. 68*, 6727−6733.
(25) Fiala, J. L., Egner, P. A., Wiriyachan, N., Ruchirawat, M., Kensler, K. H., Wogan, G. N., Groopman, J. D., Croy, R. G., and Essigmann, J. M. (2011) Sulforaphane-mediated reduction of aflatoxin B_1-N7-guanine in rat liver DNA: impacts of strain and sex. *Toxicol. Sci. 121*, 57−62.
(26) Shimada, T., and Guengerich, F. P. (1989) Evidence for cytochrome P-450NF, the nifedipine oxidase, being the principal enzyme involved in the bioactivation of aflatoxins in human liver. *Proc. Natl. Acad. Sci. U. S. A. 86*, 462−465.
(27) Raney, K. D., Shimada, T., Kim, D. H., Groopman, J. D., Harris, T. M., and Guengerich, F. P. (1992) Oxidation of aflatoxins and sterigmatocystin by human liver microsomes: significance of aflatoxin Q_1 as a detoxication product of aflatoxin B_1. *Chem. Res. Toxicol. 5*, 202−210.
(28) Ueng, Y. F., Shimada, T., Yamazaki, H., and Guengerich, F. P. (1995) Oxidation of aflatoxin B_1 by bacterial recombinant human cytochrome P450 enzymes. *Chem. Res. Toxicol. 8*, 218−225.
(29) Gallagher, E. P., Kunze, K. L., Stapleton, P. L., and Eaton, D. L. (1996) The kinetics of aflatoxin B_1 oxidation by human cDNA-expressed and human liver microsomal cytochromes P450 1A2 and 3A4. *Toxicol. Appl. Pharmacol. 141*, 595−606.
(30) Baertschi, S. W., Raney, K. D., Stone, M. P., and Harris, T. M. (1988) Preparation of the 8,9-epoxide of the mycotoxin aflatoxin B_1: the ultimate carcinogenic species. *J. Am. Chem. Soc. 110*, 7929−7931.
(31) Johnson, W. W., Harris, T. M., and Guengerich, F. P. (1996) Kinetics and mechanism of hydrolysis of aflatoxin B_1 *exo*-8,9-epoxide and rearrangement of the dihydrodiol. *J. Am. Chem. Soc. 118*, 8213−8220.
(32) Stone, M. P., Gopalakrishnan, S., Harris, T. M., and Graves, D. E. (1988) Carcinogen−nucleic acid interactions: equilibrium binding studies of aflatoxins B_1 and B_2 with DNA and the oligodeoxynucleotide $d(ATGCAT)_2$. *J. Biomol. Struct. Dyn. 5*, 1025−1041.
(33) Gopalakrishnan, S., Byrd, S., Stone, M. P., and Harris, T. M. (1989) Carcinogen−nucleic acid interactions: equilibrium binding studies of aflatoxin B_1 with the oligodeoxynucleotide $d(ATGCAT)_2$ and with plasmid *pBR322* support intercalative association with the B-DNA helix. *Biochemistry 28*, 726−734.
(34) Gopalakrishnan, S., Harris, T. M., and Stone, M. P. (1990) Intercalation of aflatoxin B_1 in two oligodeoxynucleotide adducts: comparative ^1H NMR analysis of $d(ATC^{AFB}GAT)$:d(ATCGAT) and $d(AT^{AFB}GCAT)_2$. *Biochemistry 29*, 10438−10448.
(35) Brown, K. L., Bren, U., Stone, M. P., and Guengerich, F. P. (2009) Inherent stereospecificity in the reaction of aflatoxin B_1 8,9-epoxide with deoxyguanosine and efficiency of DNA catalysis. *Chem. Res. Toxicol. 22*, 913−917.
(36) Essigmann, J. M., Croy, R. G., Nadzan, A. M., Busby, W. F., Jr., Reinhold, V. N., Buchi, G., and Wogan, G. N. (1977) Structural identification of the major DNA adduct formed by aflatoxin B_1 in vitro. *Proc. Natl. Acad. Sci. U. S. A. 74*, 1870−1874.
(37) Iyer, R. S., Coles, B. F., Raney, K. D., Thier, R., Guengerich, F. P., and Harris, T. M. (1994) DNA adduction by the potent carcinogen aflatoxin B_1: mechanistic studies. *J. Am. Chem. Soc. 116*, 1603−1609.
(38) Bren, U., Guengerich, F. P., and Mavri, J. (2007) Guanine alkylation by the potent carcinogen aflatoxin B_1: quantum chemical calculations. *Chem. Res. Toxicol. 20*, 1134−1140.
(39) Groopman, J. D., Croy, R. G., and Wogan, G. N. (1981) In vitro reactions of aflatoxin B_1-adducted DNA. *Proc. Natl. Acad. Sci. U. S. A. 78*, 5445−5449.
(40) Hertzog, P. J., Smith, J. R. L., and Garner, R. C. (1982) Characterisation of the imidazole ring-opened forms of *trans*-8,9-dihydro-8-(7-guanyl)-9-hydroxy aflatoxin B_1. *Carcinogenesis 3*, 723−725.
(41) Brown, K. L., Deng, J. Z., Iyer, R. S., Iyer, L. G., Voehler, M. W., Stone, M. P., Harris, C. M., and Harris, T. M. (2006) Unraveling the aflatoxin−FAPY conundrum: structural basis for differential replicative processing of isomeric forms of the formamidopyrimidine-type DNA adduct of aflatoxin B_1. *J. Am. Chem. Soc. 128*, 15188−15199.
(42) Smela, M. E., Hamm, M. L., Henderson, P. T., Harris, C. M., Harris, T. M., and Essigmann, J. M. (2002) The aflatoxin B_1 formamidopyrimidine adduct plays a major role in causing the types of mutations observed in human hepatocellular carcinoma. *Proc. Natl. Acad. Sci. U. S. A. 99*, 6655−6660.
(43) Bailey, E. A., Iyer, R. S., Stone, M. P., Harris, T. M., and Essigmann, J. M. (1996) Mutational properties of the primary aflatoxin B_1−DNA adduct. *Proc. Natl. Acad. Sci. U. S. A. 93*, 1535−1539.
(44) Lin, Y. C., Li, L., Makarova, A. V., Burgers, P. M., Stone, M. P., and Lloyd, R. S. (2014) Error-prone replication bypass of the primary aflatoxin B_1 DNA adduct, AFB_1-N7-Gua. *J. Biol. Chem. 289*, 18497−18506.
(45) Hertzog, P. J., Lindsay Smith, J. R., and Garner, R. C. (1980) A high pressure liquid chromatography study on the removal of DNA-bound aflatoxin B_1 in rat liver and in vitro. *Carcinogenesis 1*, 787−793.
(46) Croy, R. G., and Wogan, G. N. (1981) Temporal patterns of covalent DNA adducts in rat-liver after single and multiple doses of aflatoxin-B_1. *Cancer Res. 41*, 197−203.
(47) Bressac, B., Kew, M., Wands, J., and Ozturk, M. (1991) Selective G to T mutations of p53 in hepatocellular carcinoma from southern Africa. *Nature 350*, 429−431.
(48) Hsu, I. C., Metcalf, R. A., Sun, T., Welsh, J. A., Wang, N. J., and Harris, C. C. (1991) Mutational hotspot in the p53 gene in human hepatocellular carcinomas. *Nature 350*, 427−428.
(49) Greenblatt, M. S., Bennett, W. P., Hollstein, M., and Harris, C. C. (1994) Mutations in the p53 tumor suppressor gene: clues to cancer etiology and molecular pathogenesis. *Cancer Res. 54*, 4855−4878.
(50) Shen, H. M., and Ong, C. N. (1996) Mutations of the p53 tumor suppressor gene and ras oncogenes in aflatoxin hepatocarcinogenesis. *Mutat. Res. 366*, 23−44.

DOI: 10.1021/tx5003832
Chem. Res. Toxicol. 2015, 28, 225−237

(51) Soini, Y., Chia, S. C., Bennett, W. P., Groopman, J. D., Wang, J. S., DeBenedetti, V. M., Cawley, H., Welsh, J. A., Hansen, C., Bergasa, N. V., Jones, E. A., DiBisceglie, A. M., Trivers, G. E., Sandoval, C. A., Calderon, I. E., Munoz Espinosa, L. E., and Harris, C. C. (1996) An aflatoxin-associated mutational hotspot at codon 249 in the p53 tumor suppressor gene occurs in hepatocellular carcinomas from Mexico. *Carcinogenesis 17*, 1007−1012.

(52) Lunn, R. M., Zhang, Y. J., Wang, L. Y., Chen, C. J., Lee, P. H., Lee, C. S., Tsai, W. Y., and Santella, R. M. (1997) p53 mutations, chronic hepatitis B virus infection, and aflatoxin exposure in hepatocellular carcinoma in Taiwan. *Cancer Res. 57*, 3471−3477.

(53) Mace, K., Aguilar, F., Wang, J. S., Vautravers, P., Gomez-Lechon, M., Gonzalez, F. J., Groopman, J., Harris, C. C., and Pfeifer, A. M. (1997) Aflatoxin B_1-induced DNA adduct formation and p53 mutations in CYP450-expressing human liver cell lines. *Carcinogenesis 18*, 1291−1297.

(54) Zhang, Y. J., Rossner, P., Chen, Y., Agrawal, M., Wang, Q., Wang, L. L., Ahsan, H., Yu, M. W., Lee, P. H., and Santella, R. M. (2006) Aflatoxin B_1 and polycyclic aromatic hydrocarbon adducts, p53 mutations and p16 methylation in liver tissue and plasma of hepatocellular carcinoma patients. *Int. J. Cancer 119*, 985−991.

(55) McMahon, G., Davis, E. F., Huber, L. J., Kim, Y., and Wogan, G. N. (1990) Characterization of *c-Ki-ras* and *N-ras* oncogenes in aflatoxin B_1-induced rat liver tumors. *Proc. Natl. Acad. Sci. U. S. A. 87*, 1104−1108.

(56) Mao, H., Deng, Z., Wang, F., Harris, T. M., and Stone, M. P. (1998) An intercalated and thermally stable FAPY adduct of aflatoxin B_1 in a DNA duplex: structural refinement from ^{1}H NMR. *Biochemistry 37*, 4374−4387.

(57) Giri, I., Jenkins, M. D., Schnetz-Boutaud, N. C., and Stone, M. P. (2002) Structural refinement of the 8,9-dihydro-8-(*N*7-guanyl)-9-hydroxyaflatoxin B_1 adduct in a 5′-Cp^{AFB}G-3′ sequence. *Chem. Res. Toxicol. 15*, 638−647.

(58) Brown, K. L., Voehler, M. W., Magee, S. M., Harris, C. M., Harris, T. M., and Stone, M. P. (2009) Structural perturbations induced by the α-anomer of the aflatoxin B_1 formamidopyrimidine adduct in duplex and single-strand DNA. *J. Am. Chem. Soc. 131*, 16096−16107.

(59) Johnston, D. S., and Stone, M. P. (1995) Refined solution structure of 8,9-dihydro-8 (*N*7-guanyl)-9-hydroxy-aflatoxin B_1 opposite CpA in the complementary strand of an oligodeoxynucleotide duplex as determined by ^{1}H NMR. *Biochemistry 34*, 14037−14050.

(60) Jones, W. R., Johnston, D. S., and Stone, M. P. (1998) Refined structure of the doubly intercalated d(TAT^{AFB}GCATA)$_2$ aflatoxin B_1 adduct. *Chem. Res. Toxicol. 11*, 873−881.

(61) Adam, W., Chan, Y. Y., Cremer, D., Gauss, J., Scheutzow, D., and Schindler, M. (1987) Spectral and chemical properties of dimethyldioxirane as determined by experiment and ab initio calculations. *J. Org. Chem. 52*, 2800−2803.

(62) Adam, W., Bialas, J., and Hadjiarapoglou, L. (1991) A convenient preparation of acetone solutions of dimethyldioxirane. *Chem. Ber. 124*, 2377−2377.

(63) Murray, R. W., and Jeyaraman, R. (1985) Dioxiranes: synthesis and reactions of methyldioxiranes. *J. Org. Chem. 50*, 2847−2853.

(64) Bax, A., Griffey, R. H., and Hawkins, B. L. (1983) Correlation of proton and nitrogen-15 chemical shifts by multiple quantum NMR. *J. Magn. Reson. 55*, 301−315.

(65) Bax, A., and Summers, M. F. (1986) ^{1}H and ^{13}C assignments from sensitivity-enhanced detection of heteronuclear multiple-bond connectivity by 2D multiple quantum NMR. *J. Am. Chem. Soc. 106*, 2093−2094.

(66) Piotto, M., Saudek, V., and Sklenar, V. (1992) Gradient-tailored excitation for single-quantum NMR spectroscopy of aqueous solutions. *J. Biomol. NMR 6*, 661−665.

(67) Goddard, T. D., and Kneller, D. G. (2006) *SPARKY v. 3.113*, University of California, San Francisco, CA.

(68) Keepers, J. W., and James, T. L. (1984) A theoretical study of distance determination from NMR. Two-dimensional nuclear Overhauser effect spectra. *J. Magn. Reson. 57*, 404−426.

(69) James, T. L. (1991) Relaxation matrix analysis of two-dimensional nuclear Overhauser effect spectra. *Curr. Opin. Struct. Biol. 1*, 1042−1053.

(70) Borgias, B. A., and James, T. L. (1989) Two-dimensional nuclear Overhauser effect: complete relaxation matrix analysis. *Methods Enzymol. 176*, 169−183.

(71) Borgias, B. A., and James, T. L. (1990) MARDIGRAS—a procedure for matrix analysis of relaxation for discerning geometry of an aqueous structure. *J. Magn. Reson. 87*, 475−487.

(72) Liu, H., Spielmann, H. P., Ulyanov, N. B., Wemmer, D. E., and James, T. L. (1995) Interproton distance bounds from 2D NOE intensities: effect of experimental noise and peak integration errors. *J. Biomol. NMR 6*, 390−402.

(73) Spielmann, H. P., Dwyer, T. J., Hearst, J. E., and Wemmer, D. E. (1995) Solution structures of psoralen monoadducted and cross-linked DNA oligomers by NMR spectroscopy and restrained molecular dynamics. *Biochemistry 34*, 12937−12953.

(74) Kirkpatrick, S., Gelatt, C. D., Jr., and Vecchi, M. P. (1983) Optimization by simulated annealing. *Science 220*, 671−680.

(75) Frisch, M. J., Trucks, G. W., Schlegel, H. B., Scuseria, G. E., Robb, M. A., Cheeseman, J. R., Scalmani, G., Barone, V., Mennucci, B., Petersson, G. A., Nakatsuji, H., Caricato, M., Li, X., Hratchian, H. P., Izmaylov, A. F., Bloino, J., Zheng, G., Sonnenberg, J. L., Hada, M., Ehara, M., Toyota, K., Fukuda, R., Hasegawa, J., Ishida, M., Nakajima, T., Honda, Y., Kitao, O., Nakai, H., Vreven, T., Montgomery, J. A., Peralta, J. E., Ogliaro, F., Bearpark, M., Heyd, J. J., Brothers, E., Kudin, K. N., Staroverov, V. N., Kobayashi, R., Normand, J., Raghavachari, K., Rendell, A., Burant, J. C., Iyengar, S. S., Tomasi, J., Cossi, M., Rega, N., Millam, J. M., Klene, M., Knox, J. E., Cross, J. B., Bakken, V., Adarno, C., Jaramillo, J., Gomperts, R., Stratmann, R. E., Yazyev, O., Austin, A. J., Cammi, R., Pomelli, C., Ochterski, J. W., Martin, R. L., Morokuma, K., Zakrzewski, V. G., Voth, G. A., Salvador, P., Dannenberg, J. J., Dapprich, S., Daniels, A. D., Foresman, J. B., Ortiz, J. V., Cioslowski, J., and Fox, D. J. (2009) *GAUSSIAN09*, Gaussian, Inc., Wallingford, CT.

(76) Case, D. A., Cheatham, T. E., III, Darden, T., Gohlke, H., Luo, R., Merz, K. M., Jr., Onufriev, A., Simmerling, C., Wang, B., and Woods, R. J. (2005) The AMBER biomolecular simulation programs. *J. Comput. Chem. 26*, 1668−1688.

(77) Wang, J. M., Cieplak, P., and Kollman, P. A. (2000) How well does a restrained electrostatic potential (RESP) model perform in calculating conformational energies of organic and biological molecules? *J. Comput. Chem. 21*, 1049−1074.

(78) Bashford, D., and Case, D. A. (2000) Generalized Born models of macromolecular solvation effects. *Annu. Rev. Phys. Chem. 51*, 129−152.

(79) Tsui, V., and Case, D. A. (2000) Theory and applications of the generalized Born solvation model in macromolecular simulations. *Biopolymers 56*, 275−291.

(80) Jorgensen, W. L., Chandrasekhar, J., Madura, J. D., Impey, R. W., and Klein, M. L. (1983) Comparison of simple potential functions for simulating liquid water. *J. Chem. Phys. 79*, 926−935.

(81) Ryckaert, J.-P., Ciccotti, G., and Berendsen, H. J. C. (1977) Numerical integration of the cartesian equations of motion of a system with constraints: molecular dynamics of *n*-alkanes. *J. Comput. Phys. 23*, 327−341.

(82) Darden, T., York, D., and Pedersen, L. (1993) Particle mesh Ewald—an N.log(N) method for Ewald sums in large systems. *J. Chem. Phys. 12*, 10089−10092.

(83) Essmann, U., Perera, L., Berkowitz, M. L., Darden, T., Lee, H., and Pedersen, L. G. (1995) A smooth particle mesh Ewald method. *J. Chem. Phys. 19*, 8577−8593.

(84) Ganguly, M., Wang, F., Kaushik, M., Stone, M. P., Marky, L. A., and Gold, B. (2007) A study of 7-deaza-2′-deoxyguanosine 2′-deoxycytidine base pairing in DNA. *Nucleic Acids Res. 35*, 6181−6195.

(85) Giri, I., and Stone, M. P. (2002) Thermal stabilization of the DNA duplex by adducts of aflatoxin B_1. *Biopolymers 65*, 190−201.

(86) Patel, D. J., Shapiro, L., and Hare, D. (1987) DNA and RNA: NMR studies of conformations and dynamics in solution. *Q. Rev. Biophys. 20*, 35−112.

DOI: 10.1021/tx5003832
Chem. Res. Toxicol. 2015, 28, 225−237

(87) Reid, B. R. (1987) Sequence-specific assignments and their use in NMR studies of DNA structure. *Q. Rev. Biophys. 20*, 2−28.
(88) Boelens, R., Scheek, R. M., Dijkstra, K., and Kaptein, R. (1985) Sequential assignment of imino- and amino-proton resonances in ^{1}H NMR spectra of oligonucleotides by two-dimensional NMR spectroscopy. Application to a *lac* operator fragment. *J. Magn. Reson. 62*, 378−386.
(89) Banerjee, S., Brown, K. L., Egli, M., and Stone, M. P. (2011) Bypass of aflatoxin B_1 adducts by the *Sulfolobus solfataricus* DNA polymerase IV. *J. Am. Chem. Soc. 133*, 12556−12568.
(90) Prakash, A., Doublie, S., and Wallace, S. S. (2012) The Fpg/Nei family of DNA glycosylases: substrates, structures, and search for damage. *Prog. Mol. Biol. Transl. Sci. 110*, 71−91.
(91) Alekseyev, Y. O., Hamm, M. L., and Essigmann, J. M. (2004) Aflatoxin B_1 formamidopyrimidine adducts are preferentially repaired by the nucleotide excision repair pathway in vivo. *Carcinogenesis 25*, 1045−1051.
(92) Guo, Y., Breeden, L. L., Zarbl, H., Preston, B. D., and Eaton, D. L. (2005) Expression of a human cytochrome P450 in yeast permits analysis of pathways for response to and repair of aflatoxin-induced DNA damage. *Mol. Cell. Biol. 25*, 5823−5833.
(93) Leadon, S. A., Tyrrell, R. M., and Cerutti, P. A. (1981) Excision repair of aflatoxin B_1−DNA adducts in human fibroblasts. *Cancer Res. 41*, 5125−5129.
(94) Leadon, S. A., Zolan, M. E., and Hanawalt, P. C. (1983) Restricted repair of aflatoxin B_1 induced damage in alpha DNA of monkey cells. *Nucleic Acids Res. 11*, 5675−5689.
(95) Bedard, L. L., and Massey, T. E. (2006) Aflatoxin B_1-induced DNA damage and its repair. *Cancer Lett. 241*, 174−183.
(96) Cai, Y., Geacintov, N. E., and Broyde, S. (2012) Nucleotide excision repair efficiencies of bulky carcinogen−DNA adducts are governed by a balance between stabilizing and destabilizing interactions. *Biochemistry 51*, 1486−1499.
(97) Lukin, M., Zaliznyak, T., Johnson, F., and de los Santos, C. (2012) Structure and stability of DNA containing an aristolactam II-dA lesion: implications for the NER recognition of bulky adducts. *Nucleic Acids Res. 40*, 2759−2770.
(98) Takahashi, Y., Nakatsuru, Y., Zhang, S., Shimizu, Y., Kume, H., Tanaka, K., Ide, F., and Ishikawa, T. (2002) Enhanced spontaneous and aflatoxin-induced liver tumorigenesis in xeroderma pigmentosum group A gene-deficient mice. *Carcinogenesis 23*, 627−633.
(99) Mulder, J. E., Bondy, G. S., Mehta, R., and Massey, T. E. (2014) Up-regulation of nucleotide excision repair in mouse lung and liver following chronic exposure to aflatoxin B_1 and its dependence on p53 genotype. *Toxicol. Appl. Pharmacol. 275*, 96−103.
(100) Cai, Y., Patel, D. J., Broyde, S., and Geacintov, N. E. (2010) Base sequence context effects on nucleotide excision repair. *J. Nucleic Acids 2010*, 174252 DOI: 10.4061/2010/174252.
(101) Cai, Y., Kropachev, K., Xu, R., Tang, Y., Kolbanovskii, M., Kolbanovskii, A., Amin, S., Patel, D. J., Broyde, S., and Geacintov, N. E. (2010) Distant neighbor base sequence context effects in human nucleotide excision repair of a benzo[*a*]pyrene-derived DNA lesion. *J. Mol. Biol. 399*, 397−409.
(102) Lee, Y. C., Cai, Y., Mu, H., Broyde, S., Amin, S., Chen, X., Min, J. H., and Geacintov, N. E. (2014) The relationships between XPC binding to conformationally diverse DNA adducts and their excision by the human NER system: is there a correlation? *DNA Repair 19*, 55−63.

DOI: 10.1021/tx5003832
Chem. Res. Toxicol. 2015, 28, 225−237